A topological Dirac insulator in a quantum spin Hall phase (first experimental realization of a 3D Topological Insulator)

D. Hsieh,[1] D. Qian,[1] L. Wray,[1] Y. Xia,[1, 2] Y. S. Hor,[3] R. J. Cava,[3] and M. Z. Hasan[1, 2, 4]

[1]*Joseph Henry Laboratories of Physics, Department of Physics,*
Princeton University, Princeton, NJ 08544, USA
[2]*Princeton Center for Complex Materials, Princeton University, Princeton NJ 08544, USA*
[3]*Department of Chemistry, Princeton University, Princeton, NJ 08544, USA*
[4]*Princeton Institute for the Science and Technology of Materials (PRISM),*
*Princeton University, Princeton NJ 08544, USA**

When electrons are subject to a large external magnetic field, the conventional charge quantum Hall effect [1, 2] dictates that an electronic excitation gap is generated in the sample bulk, but metallic conduction is permitted at the boundary. Recent theoretical models suggest that certain bulk insulators with large spin-orbit interactions may also naturally support conducting topological boundary states in the extreme quantum limit [3, 4, 5], which opens up the possibility for studying unusual quantum Hall-like phenomena in zero external magnetic fields [6]. Bulk $Bi_{1-x}Sb_x$ single crystals are predicted to be prime candidates [7, 8] for one such unusual Hall phase of matter known as the topological insulator [9, 10, 11]. The hallmark of a topological insulator is the existence of metallic surface states that are higher dimensional analogues of the edge states that characterize a quantum spin Hall insulator [3, 4, 5, 6, 7, 8, 9, 10, 11, 12, 13]. In addition to its interesting boundary states, the bulk of $Bi_{1-x}Sb_x$ is predicted to exhibit three-dimensional Dirac particles [14, 15, 16, 17], another topic of heightened current interest following the new findings of two-dimensional graphene [18, 19, 20] and charge quantum Hall fractionalization observed in pure bismuth [21]. However, despite numerous transport and magnetic measurements on the $Bi_{1-x}Sb_x$ family since the 1960s [17], no direct evidence of either topological quantum Hall-like states or bulk Dirac particles has ever been found. Here, using incident-photon-energy-modulated angle-resolved photoemission spectroscopy (IPEM-ARPES), we report the direct observation of massive Dirac particles in the bulk of $Bi_{0.9}Sb_{0.1}$, locate the Kramers' points at the sample's boundary and provide a comprehensive mapping of the topological Dirac insulator's gapless surface modes. These findings taken together suggest that the observed surface state on the boundary of the bulk insulator is a realization of the much sought exotic "topological metal" [9, 10, 11]. They also suggest that this material has potential application in developing next-generation quantum computing devices that may incorporate "light-like" bulk carriers and topologically protected spin-textured edge-surface currents.

Bismuth is a semimetal with strong spin-orbit interactions. Its band structure is believed to feature an indirect negative gap between the valence band maximum at the T point of the bulk Brillouin zone (BZ) and the conduction band minima at three equivalent L points [17, 22] (here we generally refer to these as a single point, L). The valence and conduction bands at L are derived from antisymmetric (L_a) and symmetric (L_s) p-type orbitals, respectively, and the effective low-energy Hamiltonian at this point is described by the (3+1)-dimensional relativistic Dirac equation [14, 15, 16]. The resulting dispersion relation, $E(\vec{k}) = \pm\sqrt{\left(\vec{v}\cdot\vec{k}\right)^2 + \Delta^2} \approx \vec{v}\cdot\vec{k}$, is highly linear owing to the combination of an unusually large band velocity $\vec{v}$ and a small gap Δ (such that $|\Delta/|\vec{v}|| \approx 5\times10^{-3}\text{Å}^{-1}$) and has been used to explain various peculiar properties of bismuth [14, 15, 16]. Substituting bismuth with antimony is believed to change the critical energies of the band structure as follows (see Fig.1). At an Sb concentration of $x \approx 4\%$, the gap Δ between L_a and L_s closes and a massless three-dimensional (3D) Dirac point is realized. As x is further increased this gap re-opens with inverted symmetry ordering, which leads to a change in sign of Δ at each of the three equivalent L points in the BZ. For concentrations greater than $x \approx 7\%$ there is no overlap between the valence band at T and the conduction band at L, and the material becomes an inverted-band insulator. Once the band at T drops below the valence band at L, at $x \approx 8\%$, the system evolves into a direct-gap insulator whose low energy physics is dominated by the spin-orbit coupled Dirac particles at L [7, 17].

Recently, semiconductors with inverted band gaps have been proposed to manifest the two-dimensional (2D) quantum spin Hall phase, which is predicted to be characterized by the presence of metallic 1D edge states [3, 4, 5, 12]. Although a band-inversion mechanism and
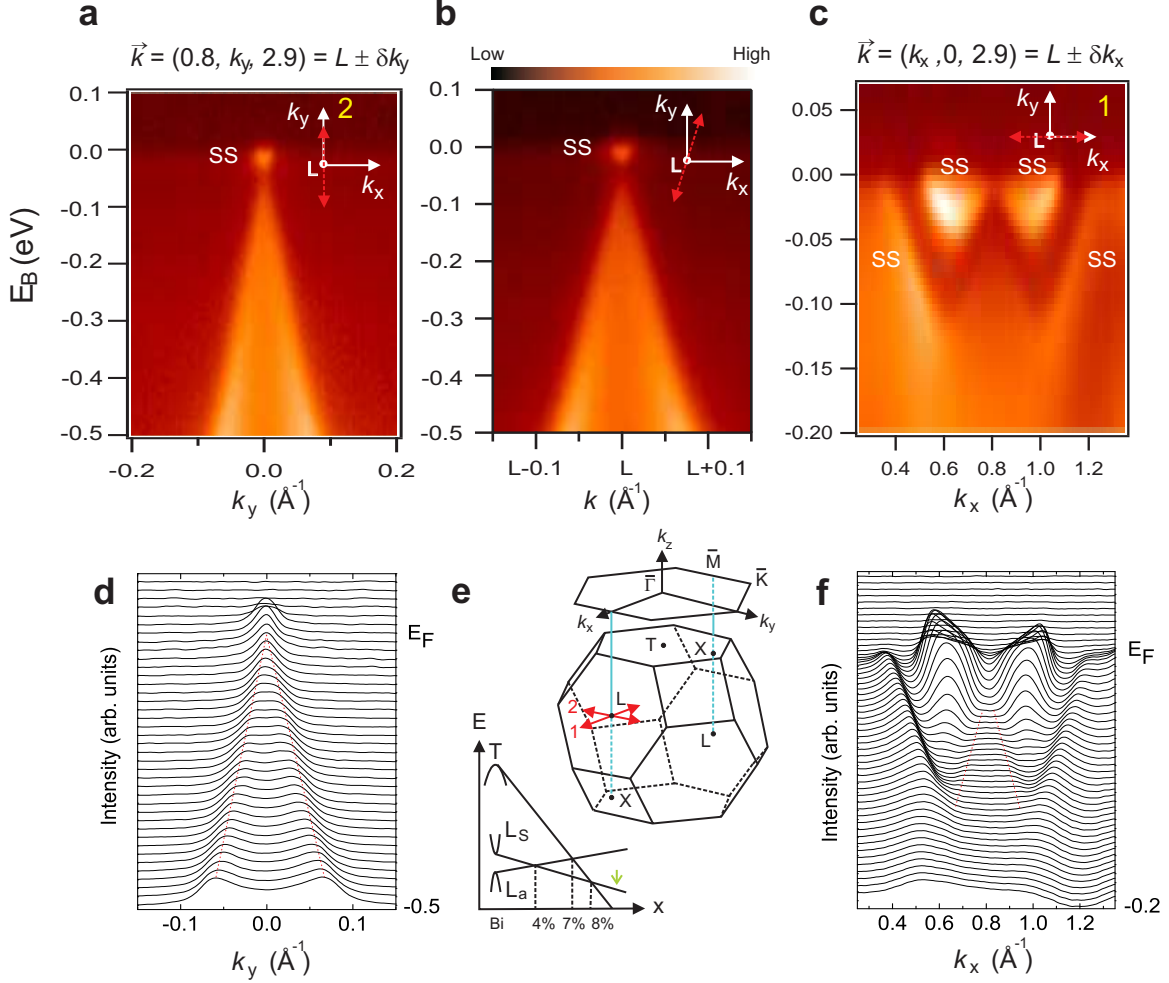
*Electronic address: mzhasan@Princeton.edu

FIG. 1: **Dirac-like dispersion near the L point in the bulk Brillouin zone.** Selected ARPES intensity maps of $Bi_{0.9}Sb_{0.1}$ are shown along three $\vec{k}$-space cuts through the L point of the bulk 3D Brillouin zone (BZ). The presented data are taken in the third BZ with $L_z = 2.9$ Å^{-1} with a photon energy of 29 eV. The cuts are along **a**, the k_y direction, **b**, a direction rotated by approximately $10°$ from the k_y direction, and **c**, the k_x direction. Each cut shows a Λ-shaped bulk band whose tip lies below the Fermi level signalling a bulk gap. The surface states are denoted SS and are all identified in Fig.2 (for further identification via theoretical calculations see Supplementary Information). **d**, Momentum distribution curves (MDCs) corresponding to the intensity map in **a**. **f**, Log scale plot of the MDCs corresponding to the intensity map in **c**. The red lines are guides to the eye for the bulk features in the MDCs. **e**, Schematic of the bulk 3D BZ of $Bi_{1-x}Sb_x$ and the 2D BZ of the projected (111) surface. The high symmetry points $\bar{\Gamma}$, $\bar{M}$ and $\bar{K}$ of the surface BZ are labeled. Schematic evolution of bulk band energies as a function of x is shown. The L band inversion transition occurs at $x \approx 0.04$, where a 3D gapless Dirac point is realized, and the composition we study here (for which $x = 0.1$) is indicated by the green arrow. A more detailed phase diagram based on our experiments is shown in Fig.3c.

edge states have been invoked to interpret the transport results in 2D mercury telluride semiconductor quantum wells [13], no 1D edge states are directly imaged, so their topological character is unknown. Recent theoretical treatments [7, 8] have focused on the strongly spin-orbit coupled, band-inverted $Bi_{1-x}Sb_x$ series as a possible 3D bulk realization of the quantum spin Hall phase in which the 1D edge states are expected to take the form of 2D surface states [7, 8, 9] that may be directly

imaged and spectroscopically studied, making it feasible to identify their topological order parameter character. Most importantly, the 3D phase is a new phase of matter in terms of its topological distinctions [10].

High-momentum-resolution angle-resolved photoemission spectroscopy performed with varying incident photon energy (IPEM-ARPES) allows for measurement of electronic band dispersion along various momentum space ($\vec{k}$-space) trajectories in the 3D bulk BZ. ARPES
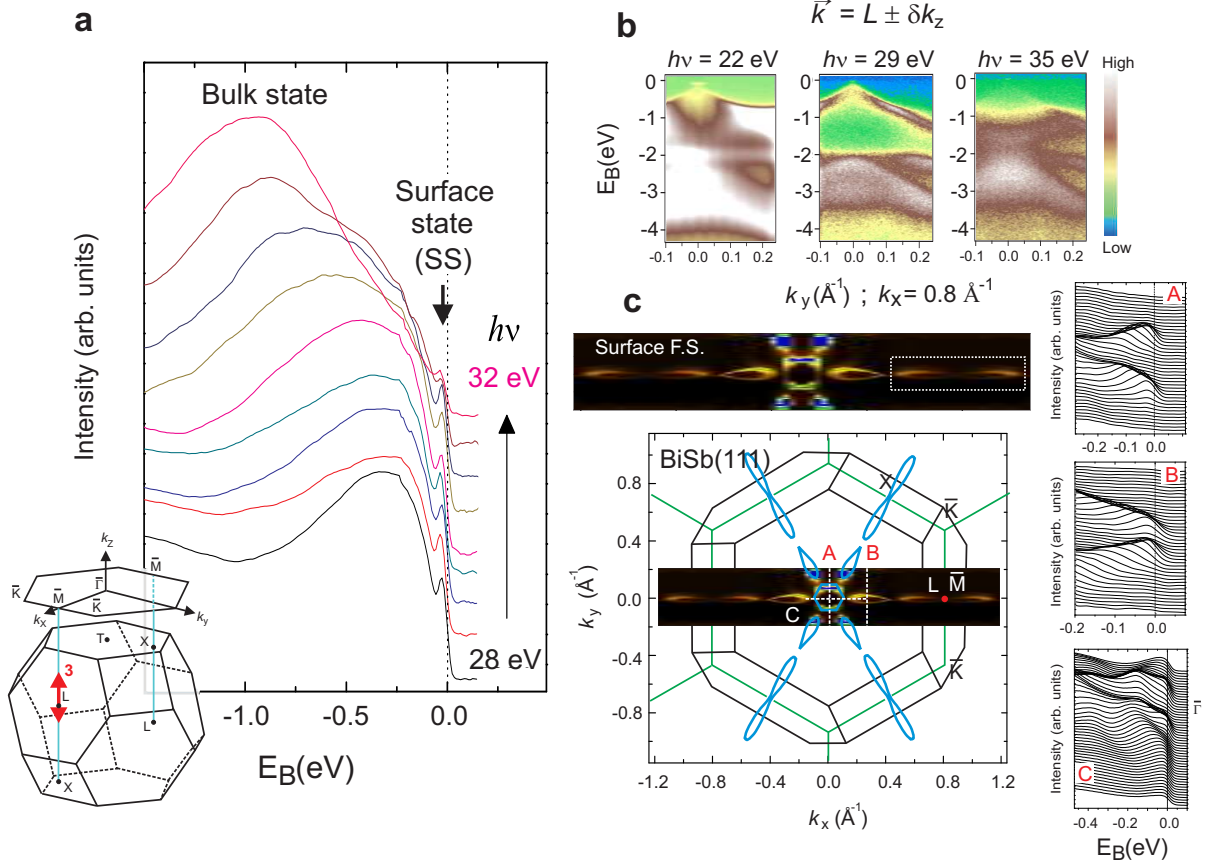
FIG. 2: **Dispersion along the cut in the k_z-direction.** Surface states are experimentally identified by studying their out-of-plane momentum dispersion through the systematic variation of incident photon energy. **a**, Energy distribution curves (EDCs) of $Bi_{0.9}Sb_{0.1}$ with electrons at the Fermi level (E_F) maintained at a fixed in-plane momentum of (k_x=0.8 Å^{-1}, k_y=0.0 Å^{-1}) are obtained as a function of incident photon energy to identify states that exhibit no dispersion perpendicular to the (111)-plane along the direction shown by the double-headed arrow labeled "3" in the inset (see Methods for detailed procedure). Selected EDC data sets with photon energies of 28 eV to 32 eV in steps of 0.5 eV are shown for clarity. The non-energy dispersive (k_z independent) peaks near E_F are the surface states (SS). **b**, ARPES intensity maps along cuts parallel to k_y taken with electrons at E_F fixed at $k_x = 0.8$ Å^{-1} with respective photon energies of $h\nu = 22$ eV, 29 eV and 35 eV (for a conversion map from photon energy to k_z see Supplementary Information). The faint Λ-shaped band at $h\nu = 22$ eV and $h\nu = 35$ eV shows some overlap with the bulk valence band at L ($h\nu = 29$ eV), suggesting that it is a resonant surface state degenerate with the bulk state in some limited k-range near E_F. The flat band of intensity centered about -2 eV in the $h\nu = 22$ eV scan originates from Bi 5d core level emission from second order light. **c**, Projection of the bulk BZ (black lines) onto the (111) surface BZ (green lines). Overlay (enlarged in inset) shows the high resolution Fermi surface (FS) of the metallic SS mode, which was obtained by integrating the ARPES intensity (taken with $h\nu = 20$ eV) from -15 meV to 10 meV relative to E_F. The six tear-drop shaped lobes of the surface FS close to $\bar{\Gamma}$ (center of BZ) show some intensity variation between them that is due to the relative orientation between the axes of the lobes and the axis of the detector slit. The six-fold symmetry was however confirmed by rotating the sample in the $k_x - k_y$ plane. EDCs corresponding to the cuts A, B and C are also shown; these confirm the gapless character of the surface states in bulk insulating $Bi_{0.9}Sb_{0.1}$.

spectra taken along two orthogonal cuts through the L point of the bulk BZ of $Bi_{0.9}Sb_{0.1}$ are shown in Figs 1a and c. A Λ-shaped dispersion whose tip lies less than 50 meV below the Fermi energy (E_F) can be seen along both directions. Additional features originating from surface states that do not disperse with incident photon energy are also seen. Owing to the finite intensity between the bulk and surface states, the exact binding energy (E_B)

where the tip of the Λ-shaped band dispersion lies is unresolved. The linearity of the bulk Λ-shaped bands is observed by locating the peak positions at higher E_B in the momentum distribution curves (MDCs), and the energy at which these peaks merge is obtained by extrapolating linear fits to the MDCs. Therefore 50 meV represents a lower bound on the energy gap Δ between L_a and L_s. The magnitude of the extracted band veloc-

ities along the k_x and k_y directions are $7.9 \pm 0.5 \times 10^4$ ms^{-1} and $10.0 \pm 0.5 \times 10^5$ ms^{-1}, respectively, which are similar to the tight binding values 7.6×10^4 ms^{-1} and 9.1×10^5 ms^{-1} calculated for the L$_a$ band of bismuth [22]. Our data are consistent with the extremely small effective mass of $0.002m_e$ (where m_e is the electron mass) observed in magneto-reflection measurements on samples with $x = 11\%$ [23]. The Dirac point in graphene, co-incidentally, has a band velocity ($|v_F| \approx 10^6$ ms^{-1}) [18] comparable to what we observe for Bi$_{0.9}$Sb$_{0.1}$, but its spin-orbit coupling is several orders of magnitude weaker [3], and the only known method of inducing a gap in the Dirac spectrum of graphene is by coupling to an external chemical substrate [20]. The Bi$_{1-x}$Sb$_x$ series thus provides a rare opportunity to study relativistic Dirac Hamiltonian physics in a 3D condensed matter system where the intrinsic (rest) mass gap can be easily tuned.

Studying the band dispersion perpendicular to the sample surface provides a way to differentiate bulk states from surface states in a 3D material. To visualize the near-E_F dispersion along the 3D L-X cut (X is a point that is displaced from L by a k_z distance of $3\pi/c$, where c is the lattice constant), in Fig.2a we plot energy distribution curves (EDCs), taken such that electrons at E_F have fixed in-plane momentum $(k_x, k_y) = (L_x, L_y) = (0.8 \text{ Å}^{-1}, 0.0 \text{ Å}^{-1})$, as a function of photon energy ($h\nu$). There are three prominent features in the EDCs: a non-dispersing, k_z independent, peak centered just below E_F at about -0.02 eV; a broad non-dispersing hump centered near -0.3 eV; and a strongly dispersing hump that coincides with the latter near $h\nu = 29$ eV. To understand which bands these features originate from, we show ARPES intensity maps along an in-plane cut $\bar{K}\bar{M}\bar{K}$ (parallel to the k_y direction) taken using $h\nu$ values of 22 eV, 29 eV and 35 eV, which correspond to approximate k_z values of L$_z -$ 0.3 Å^{-1}, L$_z$, and L$_z$ + 0.3 Å^{-1} respectively (Fig.2b). At $h\nu = 29$ eV, the low energy ARPES spectral weight reveals a clear Λ-shaped band close to E_F. As the photon energy is either increased or decreased from 29 eV, this intensity shifts to higher binding energies as the spectral weight evolves from the Λ-shaped into a $\cup$-shaped band. Therefore the dispersive peak in Fig.2a comes from the bulk valence band, and for $h\nu = 29$ eV the high symmetry point L = (0.8, 0, 2.9) appears in the third bulk BZ. In the maps of Fig.2b with respective $h\nu$ values of 22 eV and 35 eV, overall weak features near E_F that vary in intensity remain even as the bulk valence band moves far below E_F. The survival of these weak features over a large photon energy range (17 to 55 eV) supports their surface origin. The non-dispersing feature centered near -0.3 eV in Fig.2a comes from the higher binding energy (valence band) part of the full spectrum of surface states, and the weak non-dispersing peak at -0.02 eV reflects the low energy part of the surface states that cross E_F away from the $\bar{M}$ point and forms the surface Fermi surface (Fig.2c).

Having established the existence of an energy gap in the bulk state of Bi$_{0.9}$Sb$_{0.1}$ (Figs 1 and 2) and ob-

served linearly dispersive bulk bands uniquely consistent with strong spin-orbit coupling model calculations [14, 15, 16, 22] (see Supplementary Information for full comparison with theoretical calculation), we now discuss the topological character of its surface states, which are found to be gapless (Fig.2c). In general, the states at the surface of spin-orbit coupled compounds are allowed to be spin split owing to the loss of space inversion symmetry $[E(k,\uparrow) = E(-k,\uparrow)]$. However, as required by Kramers' theorem, this splitting must go to zero at the four time reversal invariant momenta (TRIM) in the 2D surface BZ. As discussed in [7, 9], along a path connecting two TRIM in the same BZ, the Fermi energy inside the bulk gap will intersect these singly degenerate surface states either an even or odd number of times. When there are an even number of surface state crossings, the surface states are topologically trivial because weak disorder (as may arise through alloying) or correlations can remove *pairs* of such crossings by pushing the surface bands entirely above or below E_F. When there are an odd number of crossings, however, at least one surface state must remain gapless, which makes it non-trivial [7, 8, 9]. The existence of such topologically non-trivial surface states can be theoretically predicted on the basis of the *bulk* band structure only, using the Z_2 invariant that is related to the quantum Hall Chern number [24]. Materials with band structures with $Z_2 = +1$ are ordinary Bloch band insulators that are topologically equivalent to the filled shell atomic insulator, and are predicted to exhibit an even number (including zero) of surface state crossings. Materials with bulk band structures with $Z_2 = -1$ on the other hand, which are expected to exist in rare systems with strong spin-orbit coupling acting as an internal quantizing magnetic field on the electron system [6], and inverted bands at an odd number of high symmetry points in their bulk 3D BZs, are predicted to exhibit an odd number of surface state crossings, precluding their adiabatic continuation to the atomic insulator [3, 7, 8, 9, 10, 11, 12, 13]. Such "topological quantum Hall metals" [9, 10, 11] cannot be realized in a purely 2D electron gas system such as the one realized at the interface of GaAs/GaAlAs systems.

In our experimental case, namely the (111) surface of Bi$_{0.9}$Sb$_{0.1}$, the four TRIM are located at $\bar{\Gamma}$ and three $\bar{M}$ points that are rotated by 60° relative to one another. Owing to the three-fold crystal symmetry (A7 bulk structure) and the observed mirror symmetry of the surface Fermi surface across $k_x = 0$ (Fig.2), these three $\bar{M}$ points are equivalent (and we henceforth refer to them as a single point, $\bar{M}$). The mirror symmetry $[E(k_y) = E(-k_y)]$ is also expected from time reversal invariance exhibited by the system. The complete details of the surface state dispersion observed in our experiments along a path connecting $\bar{\Gamma}$ and $\bar{M}$ are shown in Fig.3a; finding this information is made possible by our experimental separation of surface states from bulk states. As for bismuth (Bi), two surface bands emerge from the bulk band continuum near $\bar{\Gamma}$ to form a central electron pocket and an adjacent
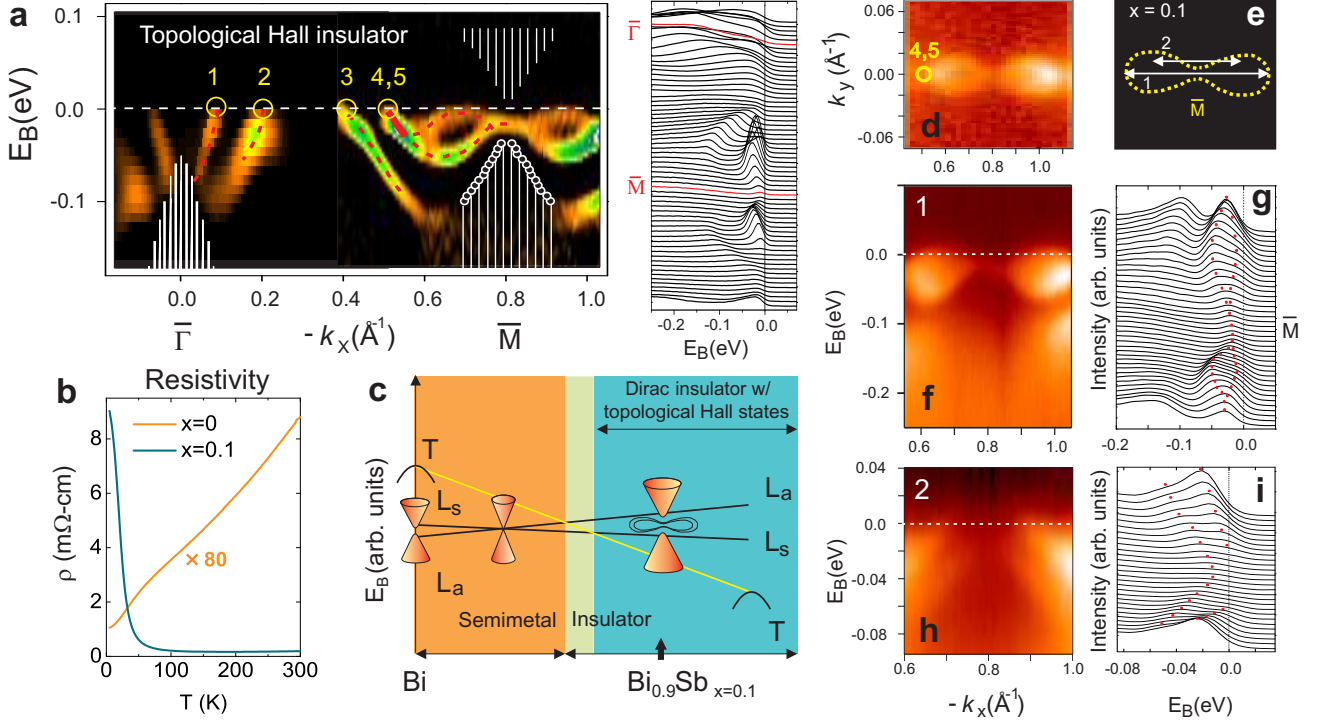
FIG. 3: **The topological gapless surface states in bulk insulating Bi$_{0.9}$Sb$_{0.1}$. a**, The surface band dispersion second derivative image (SDI) of Bi$_{0.9}$Sb$_{0.1}$ along $\bar{\Gamma} - \bar{M}$. The shaded white area shows the projection of the bulk bands based on ARPES data, as well as a rigid shift of the tight binding bands to sketch the unoccupied bands above the Fermi level. To maintain high momentum resolution, data were collected in two segments of momentum space, then the intensities were normalized using background level above the Fermi level. A non-intrinsic flat band of intensity near E_F generated by the SDI analysis was rejected to isolate the intrinsic dispersion. The Fermi crossings of the surface state are denoted by yellow circles, with the band near $-k_x \approx 0.5$ Å^{-1} counted twice owing to double degeneracy. The red lines are guides to the eye. An in-plane rotation of the sample by 60° produced the same surface state dispersion. The EDCs along $\bar{\Gamma} - \bar{M}$ are shown to the right. There are a total of five crossings from $\bar{\Gamma} - \bar{M}$ which indicates that these surface states are topologically non-trivial. The number of surface state crossings in a material (with an odd number of Dirac points) is related to the topological Z_2 invariant (see text). **b**, The resistivity curves of Bi and Bi$_{0.9}$Sb$_{0.1}$ reflect the contrasting transport behaviours. The presented resistivity curve for pure bismuth has been multiplied by a factor of 80 for clarity. **c**, Schematic variation of bulk band energies of Bi$_{1-x}$Sb$_x$ as a function of x (based on band calculations and on [7, 17]). Bi$_{0.9}$Sb$_{0.1}$ is a direct gap bulk Dirac point insulator well inside the inverted-band regime, and its surface forms a "topological metal" - the 2D analogue of the 1D edge states in quantum spin Hall systems. **d**, ARPES intensity integrated within ± 10 meV of E_F originating solely from the surface state crossings. The image was plotted by stacking along the negative k_x direction a series of scans taken parallel to the k_y direction. **e**, Outline of Bi$_{0.9}$Sb$_{0.1}$ surface state ARPES intensity near E_F measured in **d**. White lines show scan directions "1" and "2". **f**, Surface band dispersion along direction "1" taken with $h\nu = 28$ eV and the corresponding EDCs (**g**). The surface Kramers degenerate point, critical in determining the topological Z_2 class of a band insulator, is clearly seen at $\bar{M}$, approximately 15 ± 5 meV below E_F. (We note that the scans are taken along the negative k_x direction, away from the bulk L point.) **h**, Surface band dispersion along direction "2" taken with $h\nu = 28$ eV and the corresponding EDCs (**i**). This scan no longer passes through the $\bar{M}$-point, and the observation of two well separated bands indicates the absence of Kramers degeneracy as expected, which cross-checks the result in (**a**).

hole lobe [25, 26, 27]. It has been established that these two bands result from the spin-splitting of a surface state and are thus singly degenerate [27, 28]. On the other hand, the surface band that crosses E_F at $-k_x \approx 0.5$ Å^{-1}, and forms the narrow electron pocket around $\bar{M}$, is clearly doubly degenerate, as far as we can determine within our experimental resolution. This is indicated by

its splitting below E_F between $-k_x \approx 0.55$ Å^{-1} and $\bar{M}$, as well as the fact that this splitting goes to zero at $\bar{M}$ in accordance with Kramers theorem. In semimetallic single crystal bismuth, only a single surface band is observed to form the electron pocket around $\bar{M}$ [29, 30]. Moreover, this surface state overlaps, hence becomes degenerate with, the bulk conduction band at L (L projects

to the surface $\bar{M}$ point) owing to the semimetallic character of Bi (Fig.3b). In $\mathrm{Bi}_{0.9}\mathrm{Sb}_{0.1}$ on the other hand, the states near $\bar{M}$ fall completely inside the bulk energy gap preserving their purely surface character at $\bar{M}$ (Fig.3a). The surface Kramers doublet point can thus be defined in the bulk insulator (unlike in Bi [25, 26, 27, 28, 29, 30]) and is experimentally located in $\mathrm{Bi}_{0.9}\mathrm{Sb}_{0.1}$ samples to lie approximately 15 ± 5 meV below E_F at $\vec{k} = \bar{M}$ (Fig.3a). For the precise location of this Kramers point, it is important to demonstrate that our alignment is strictly along the $\bar{\Gamma} - \bar{M}$ line. To do so, we contrast high resolution ARPES measurements taken along the $\bar{\Gamma} - \bar{M}$ line with those that are slightly offset from it (Fig.3e). Figs 3f-i show that with k_y offset from the Kramers point at $\bar{M}$ by less than 0.02 Å^{-1}, the degeneracy is lifted and only one band crosses E_F to form part of the bow-shaped electron distribution (Fig.3d). Our finding of five surface state crossings (an odd rather than an even number) between $\bar{\Gamma}$ and $\bar{M}$ (Fig.3a), confirmed by our observation of the Kramers degenerate point at the TRIM, indicates that these gapless surface states are topologically non-trivial. This corroborates our bulk electronic structure result that $\mathrm{Bi}_{0.9}\mathrm{Sb}_{0.1}$ is in the insulating band-inverted ($Z_2 = -1$) regime (Fig.3c), which contains an odd number of bulk (gapped) Dirac points, and is topologically analogous to an integer quantum spin Hall insulator.

Our experimental results taken collectively strongly suggest that $\mathrm{Bi}_{0.9}\mathrm{Sb}_{0.1}$ is quite distinct from graphene [18, 19] and represents a novel state of quantum matter: a strongly spin-orbit coupled insulator with an odd number of Dirac points with a negative Z_2 topological Hall phase, which realizes the "parity anomaly without Fermion doubling". Our work further demonstrates a general methodology for possible future investigations of *novel topological orders* in exotic quantum matter.

Note Added : In a very recent work we have successfully imaged the spin-polarization of the topological edge modes using high-resolution spin-resolved-ARPES [39].

Author information Correspondence and requests for materials should be addressed to M.Z.H (mzhasan@princeton.edu).

METHODS SUMMARY

High resolution IPEM-ARPES data have been taken at Beamlines 12.0.1 and 10.0.1 of the Advanced Light Source in Lawrence Berkeley National Laboratory, as well as at PGM Beamline of the Synchrotron Radiation Center in Wisconsin, with photon energies from 17 to 55 eV and energy resolution from 9 to 40 meV and momentum (k-)resolution better than 1.5% of the surface Brillouin zone. Data were taken on high quality bulk single crystal $\mathrm{Bi}_{1-x}\mathrm{Sb}_x$ at a temperature of 15 K and chamber pressures better than 8×10^{-11} torr. Throughout this paper, the bulk bands presented are from those measured in the third bulk Brillouin zone to ensure a high degree of signal-to-noise contrast, and the k_z values are estimated using the standard free-electron final state approximation.

SUPPLEMENTARY INFORMATION

METHODS

Growth method for high-quality single crystals

The $\mathrm{Bi}_{1-x}\mathrm{Sb}_x$ single-crystal samples ($0 \leq x \leq 0.17$) used for ARPES experiments were each cleaved from a boule grown from a stoichiometric mixture of high-purity elements. The boule was cooled from 650 °C to 270 °C over a period of five days and was annealed for seven days at 270 °C. The samples naturally cleaved along the (111) plane, which resulted in shiny flat silver surfaces. X-ray diffraction measurements were used to check that the samples were single phase, and confirmed that the $\mathrm{Bi}_{0.9}\mathrm{Sb}_{0.1}$ single crystals presented in this paper have a rhombohedral A7 crystal structure (point group $R\bar{3}m$), with room-temperature (T=300K) lattice parameters $a = 4.51$ Å and $c = 11.78$ Å indexed using a rhombohedral unit cell. The X-ray diffraction patterns of the cleaved crystals exhibit only the (333), (666), and (999) peaks, showing that the cleaved surface is oriented along the trigonal (111) axis. Room-temperature data were recorded on a Bruker D8 diffractometer using Cu Kα radiation ($\lambda = 1.54$ Å) and a diffracted-beam monochromator. The in-plane crystal orientation was determined by Laue X-ray diffraction. During the angle-resolved photoemission spectroscopy (ARPES) measurements a fine alignment was achieved by carefully studying the band dispersions and Fermi surface symmetry as an internal check for crystal orientation.

Transport measurements

Temperature-dependent resistivity measurements were carried out on single-crystal samples in a Quantum Design PPMS-9 instrument, using a standard four-probe technique on approximately $4 \times 1 \times 1$-mm^3, rectangular samples with the current in the basal plane, which was perpendicular to the trigonal axis. The four contacts were made by using room-temperature silver paste. The data for samples with concentrations ranging from $x = 0$ to $x = 0.17$ showed a systematic change from semimetallic to insulating-like behaviour with increasing x, in agreement with previously published works[15], which was used as a further check of the antimony concentrations. Conventional magnetic and transport measurements[7,17,31] such as these cannot separately measure the contributions of the surface and bulk states to the total signal. ARPES, on the other hand, is a momentum-selective technique[32], which allows for a separation of 2D (surface) from 3D (bulk) dispersive energy bands. This capability is especially important for $\mathrm{Bi}_{1-x}\mathrm{Sb}_x$ because the Dirac point lies at a single point in the 3D Brillouin zone, unlike for 2D
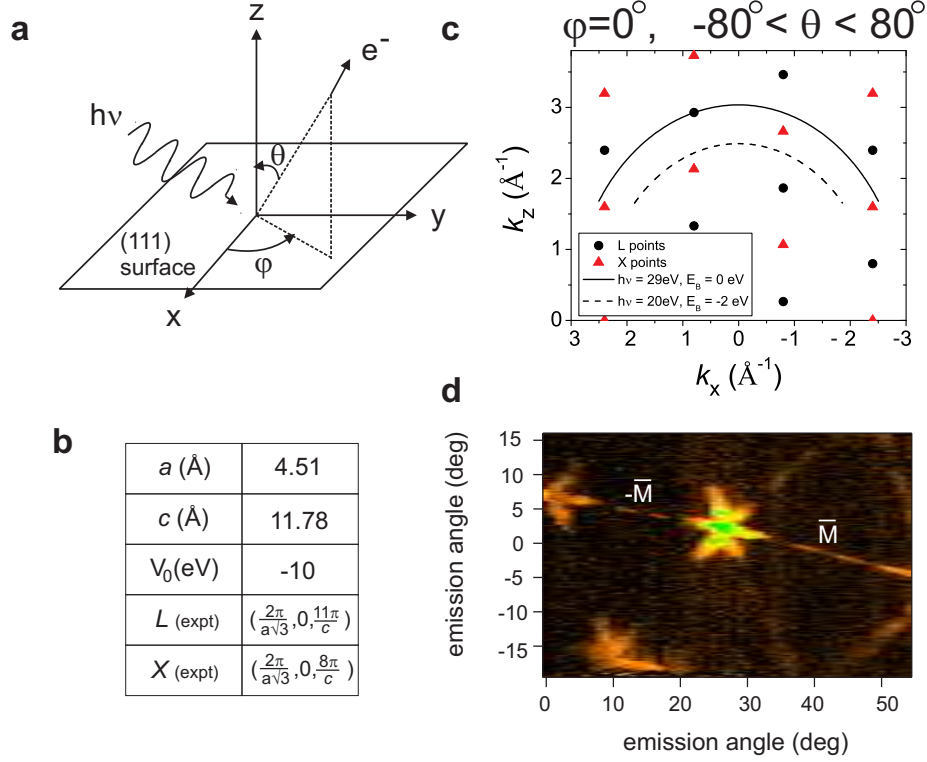
FIG. S1: **Method of locating high symmetry bulk reciprocal lattice points of Bi$_{0.9}$Sb$_{0.1}$ using incident photon energy modulated ARPES. a,** Geometry of an ARPES experiment. **b,** Key parameters relevant to the calculation of the positions of the high symmetry points in the 3D BZ. The lattice constants refer to the rhombohedral A7 lattice structure. **c,** Location of L and X points of the bulk BZ in the k_x-k_z plane together with the constant energy contours that can be accessed by changing the angle θ. **d,** Near E_F intensity map ($h\nu = 55$ eV) of the Fermi surface formed by the surface states covering an entire surface BZ, used to help locate various in-plane momenta, in units of the photoelectron emission angle along two orthogonal spatial directions. The electron pockets near $\bar{M}$ in Fig.2c (main text) appear as lines in Fig.S1d due to relaxed k-resolution in order to cover a large k-space in a single shot.

graphene, where the Dirac points can be studied at any arbitrary perpendicular momentum along a line[33,34].

$$|E_B| = h\nu - W - E_{kin}$$
$$k_x = K_x = \frac{1}{\hbar}\sqrt{2m_e E_{kin}}\sin\theta$$
$$k_z = \frac{1}{\hbar}\sqrt{2m_e(E_{kin}\cos^2\theta - V_0)}$$

where we have set $\varphi = 0$, W is the work function, m_e is the electron mass and V_0 is an experimentally determined parameter, which is approximately -10 eV for bismuth[35,36]. Features in the ARPES spectra originating from bulk initial states (dispersive along the k_z-direction) were distinguished from those originating from surface initial states (non-dispersive along the k_z-direction) by studying their dependence on incident photon energy, $h\nu$, and converting this to dependence on k_z via the displayed equations. ARPES data were collected at beamlines 12.0.1 and 10.0.1 of the Advanced Light Source at the Lawrence Berkeley National Laboratory, as well as at the PGM beamline of the Synchrotron Radiation Center in Wisconsin, with incident photon energies ranging from 17 eV to 55 eV, energy resolutions ranging from 9 meV to 40 meV and momentum resolution better than 1.5% of the surface Brillouin zone, using Scienta electron analysers. The combination of high spatial resolution and high crystalline

Systematic methods for separating bulk from surface electronic states

ARPES is a photon-in, electron-out technique[32]. Photoelectrons ejected from a sample by a monochromatic beam of radiation are collected by a detector capable of measuring its kinetic energy E_{kin}. By varying the detector angles, θ and φ, relative to the sample surface normal, the momentum of the photoelectrons, $\mathbf{K}$, can also be determined (as illustrated in Supplementary Fig. 1a). By employing the commonly used free-electron final state approximation, we can fully convert from the measured kinetic energy and momentum values of the photoelectron to the binding energy, E_B, and Bloch momentum values $\mathbf{k}$ of its initial state inside the crystal, via
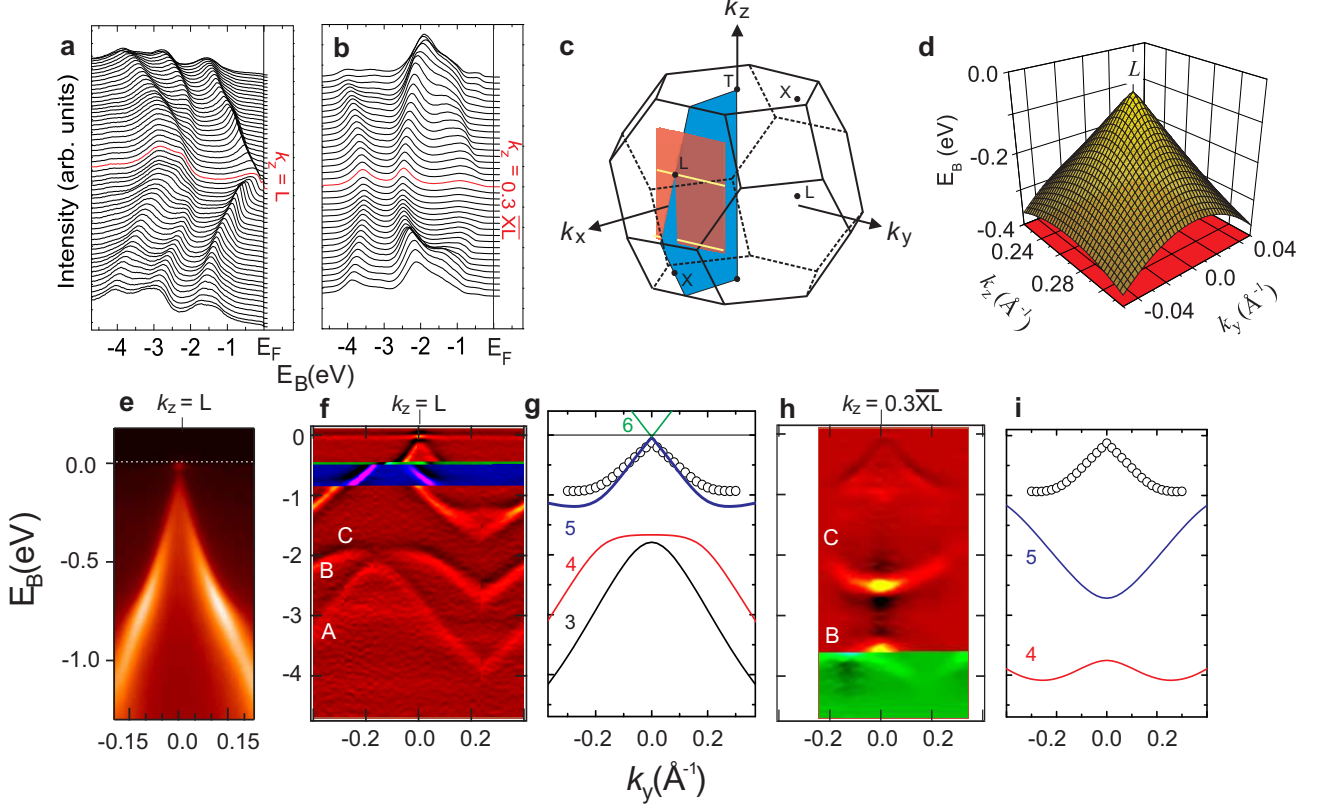
FIG. S2: **Identification of the bulk band features of $Bi_{0.9}Sb_{0.1}$. Experimental band-structure determined by ARPES is compared to bulk tight-binding calculations of bismuth to further identify the deeper lying bulk bands and their symmetry origins. a,** Energy distribution curves (EDCs) along a k-space cut given by the upper yellow line shown in schematic **c** which goes through the bulk L point in the 3rd BZ ($h\nu = 29$ eV). The corresponding ARPES intensity in the vicinity of L is shown in **e**. **b,** EDCs along the lower yellow line of **c** which goes through the point a fraction 0.3 of the k-distance from X to L ($h\nu = 20$ eV), showing a dramatic change of the deeper lying band dispersions. (This cut was taken at a k_x value equal in magnitude but opposite in sign to that in **a** as described in the SI text). **f,h,** The ARPES second derivative images (SDI) of the raw data shown in **a** and **b** to reveal the band dispersions. The flat band of intensity at E_F is an artifact of taking SDI. **g,i,** Tight binding band calculations of bismuth including spin-orbit coupling, using Liu and Allen model[22], along the corresponding experimental cut directions shown in **f** and **h**. The bands (colored solid lines) labelled 3 to 6 are derived from the symmetries associated with the $6p$-orbitals and their dispersion is thus strongly influenced by spin-orbit coupling. The inter-band gap between bands 5 and 6 is barely visible on the scale of Fig. S2g. The circled curves mark the surface state dispersion, which is present at all measured photon energies (no k_z dispersion). There is a close match of the bulk band dispersion between the data and calculations, confirming the presence of strong spin-orbit coupling. **d,** Tight binding valence band (5) dispersion of bismuth in the k_y-k_z momentum plane showing linearity along both directions. The close match between data and calculation along k_y suggests that the dispersion near E_F along k_z is also linear.

quality enabled us to probe only the highly ordered and cleanest regions of our samples. Single-crystal $Bi_{1-x}Sb_x$ samples were cleaved in situ at a temperature of 15 K and chamber pressures less than 8×10^{-11} torr, and high surface quality was checked throughout the measurement process by monitoring the EDC linewidths of the surface state. To measure the near-E_F dispersion of an electronic band along a direction normal to the sample surface, such as the direction from $X(2\pi/\sqrt{3}a, 0, 8\pi/c)$ to $L(2\pi/\sqrt{3}a, 0, 11\pi/c)$ shown in Fig. 2a, EDCs were taken at several incident photon energies. The kinetic energy of the photoelectron at E_F is different for each value of $h\nu$, so the angle was first adjusted and then held fixed for each $h\nu$ so as to keep k_x constant at $2\pi/\sqrt{3}a = 0.8$ Å^{-1} for

electrons emitted near E_F. To ensure that the in-plane momentum remained constant at $\bar{M}$ (the L-X line projects onto $\bar{M}$) for each EDC, a complete near-E_F intensity map was generated for each photon energy to precisely locate the $\bar{M}$-point (see Supplementary Fig. 1d). We note that because the bulk crystal has only three-fold rotational symmetry about the k_z-axis, the reciprocal lattice does not have mirror symmetry about the $k_x = 0$ plane. Therefore, scans taken at $+\theta$ and $-\theta$ for the same photon energy probe different points in the bulk 3D Brillouin zone; this is responsible for the absence of the bulk Λ-shaped band in Fig. 3f.

Tight binding bandstructure near L point
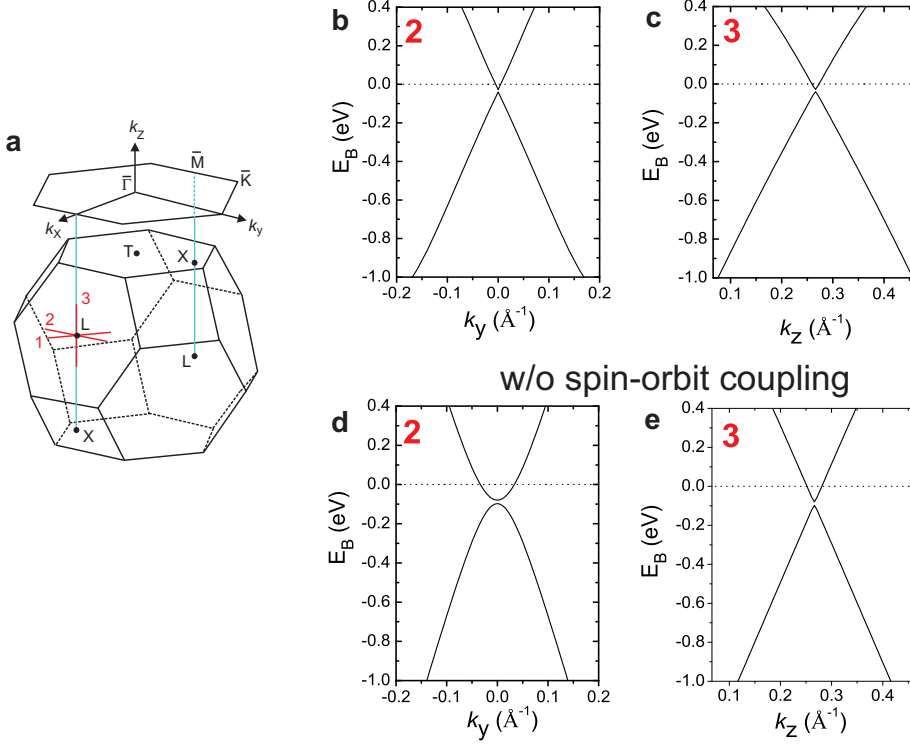## w/ spin-orbit coupling

w/o spin-orbit coupling

FIG. S3: **Spin-orbit coupling has a profound effect on the band structure of bismuth near L point. a,** Schematic of the bulk 3D BZ and the projected BZ of the (111) surface. **b,c,** Calculated tight binding band structure of bismuth including a spin-orbit coupling strength of 1.5 eV [22] along two orthogonal cuts through the L point in the 1st bulk BZ. **d,e,** Tight binding band structure along the same two directions as **b** and **c** calculated without spin-orbit coupling. The inter-band gap of 13.7 meV is barely visible on the scale of **b** and **c**.

CONFIRMING THE BULK NATURE OF ELECTRONIC BANDS BY COMPARISON WITH THEORETICAL CALCULATIONS

In an ARPES experiment (Fig.S1a), three dimensional (3D) dispersive bulk electronic states can be identified as those that disperse with incident photon energy, whereas surface states do not. As an additional check that we have indeed correctly identified the bulk bands of $Bi_{0.9}Sb_{0.1}$ in Figs 1 and 2, we also measured the dispersion of the deeper lying bands well below the Fermi level (E_F) and compared them to tight binding theoretical calculations of the bulk bands of pure bismuth following the model of Liu and Allen (1995)[22]. A tight-binding approach is known to be valid since $Bi_{0.9}Sb_{0.1}$ is not a strongly correlated electron system. As $Bi_{0.9}Sb_{0.1}$ is a random alloy (Sb does not form a superlattice[17]) with a relatively small Sb concentration (∼0.2 Sb atoms per rhombohedral unit cell), the deeper lying band structure of $Bi_{0.9}Sb_{0.1}$ is expected to follow that of pure Bi because the deeper lying (localized wave function) bands of $Bi_{0.9}Sb_{0.1}$ are not greatly affected by the substitutional disorder, and no additional back folded bands are expected to arise. Since these deeper lying bands are predicted to change dramatically with k_z, they help

us to finely determine the experimentally probed k_z values. Fig.S2f shows the ARPES second derivative image (SDI) of a cut parallel to $\bar{K}\bar{M}\bar{K}$ that passes through the L point of the 3D Brillouin zone (BZ), and Fig.S2h shows a parallel cut that passes through the 0.3 XL point (Fig.S2c). The locations of these two cuts in the 3D bulk BZ were calculated from the kinematic relations described in the Methods section, from which we can construct the constant energy contours shown in Fig. S1c. By adjusting θ such that the in-plane momentum k_x is fixed at approximately 0.8 Å^{-1} (the surface $\bar{M}$ point), at a photon energy $h\nu$ =29 eV, electrons at the Fermi energy (E_B=0 eV) have a k_z that corresponds to the L point in the 3rd bulk BZ. By adjusting θ such that the in-plane momentum k_x is fixed at approximately -0.8 Å^{-1}, at a photon energy $h\nu = 20$ eV, electrons at a binding energy of -2 eV have a k_z near 0.3 XL.

There is a clear k_z dependence of the dispersion of measured bands A, B and C, pointing to their bulk nature. The bulk origin of bands A, B and C is confirmed by their good agreement with tight binding calculations (bands 3, 4 and 5 in Figs S2g and i), which include a strong spin-orbit coupling constant of 1.5 eV derived from bismuth[22]. Band 3 drops below -5 eV at the 0.3 XL point. The slight differences
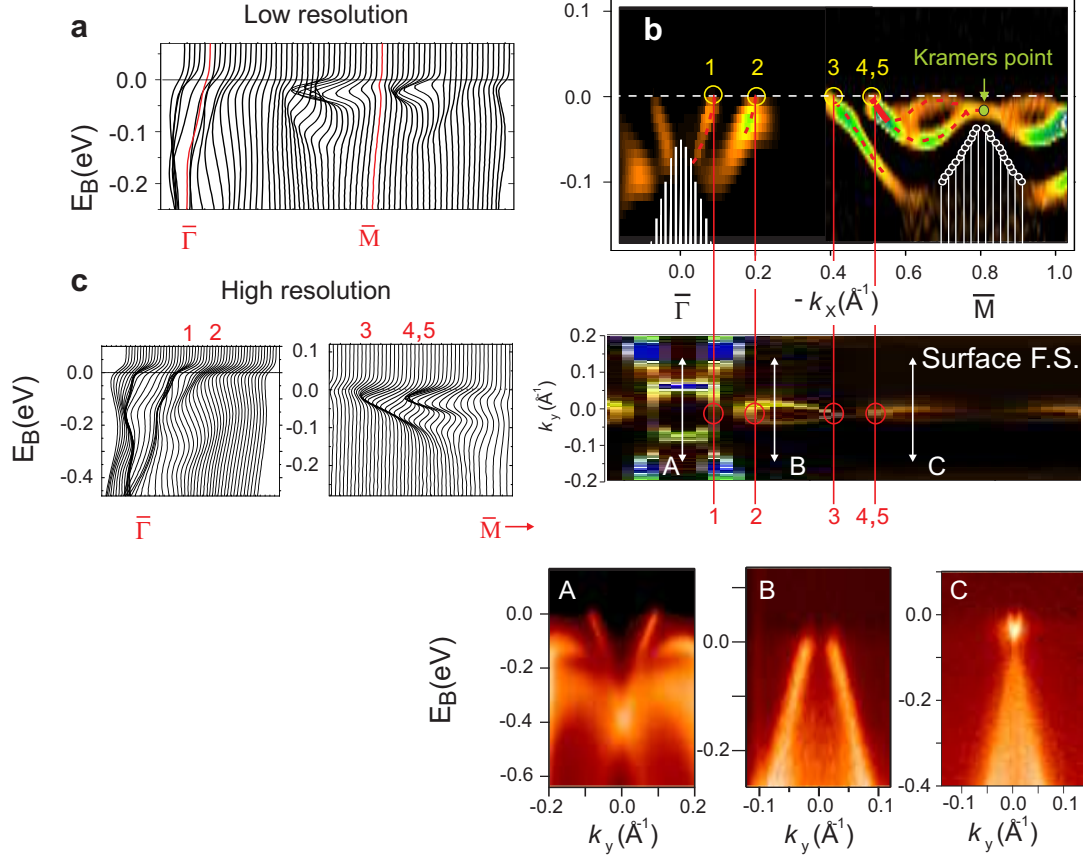
FIG. S4: **The Kramers' point, the gapless nature and topology of surface states in insulating Bi$_{0.9}$Sb$_{0.1}$ is revealed through high spatial and k-resolution ARPES. a,** Energy distribution curves (EDCs) of a low resolution ARPES scan along the surface $\bar{\Gamma}$-$\bar{M}$ cut of Bi$_{0.9}$Sb$_{0.1}$. **b,** The surface band dispersion second derivative image along $\bar{\Gamma}$-$\bar{M}$ obtained by piecing together four high resolution ARPES scans. See main text Fig.3 for explanation of other features. **c,** EDCs of high resolution ARPES scans in the vicinity of surface Fermi crossings 1 and 2 and crossings 3, 4 and 5 (left panels). These crossings form the surface Fermi surface shown in the upper right panel of **c** (see also main text Fig.2). High resolution ARPES scans along cut directions A, B and C are further evidence for a surface Fermi surface.

between the experimentally measured band energies and the calculated band energies at $k_y = 0$ Å^{-1} shown in Fig.S2f-i are due to the fact that the ARPES data were collected in a single shot, taken in constant θ mode. This means that electrons detected at different binding energies will have slightly different values of k_z as described in Methods, whereas the presented tight binding calculations show all bands at a single k_z. We checked that the magnitude of these band energy differences is indeed accounted for by this explanation. Even though the L_a and L_s bands in Bi$_{0.9}$Sb$_{0.1}$ are inverted relative to those of pure semimetallic Bi, calculations show that near E_F, apart from an insulating gap, they are "mirror" bands in terms of k dispersion (see bands 5 and 6 in Fig.S2g). Such a close match to calculations, which also predict a linear dispersion along the k_z cut near E_F (Fig.S2d), provides strong support that the dispersion of band C, near E_F, is in fact linear along k_z. Focusing on the Λ-shaped valence band at L, the EDCs (Fig.S2a) show a single peak out to $k_y \approx \pm 0.15$ Å^{-1} demonstrating that it is composed of a single band feature. Outside this range however, an additional feature develops on

the low binding energy side of the main peak in the EDCs, which shows up as two well separated bands in the SDI image (Fig.2f) and signals a splitting of the band into bulk representative and surface representative components (Fig.S2a,f). Unlike the main peak that disperses strongly with incident photon energy, this shoulder-like feature is present and retains the same Λ-shaped dispersion near this k-region (open circles in Figs S2g and i) for all photon energies used, supporting its 2D surface character. This behaviour is quite unlike bulk band C, which attains the Λ-shaped dispersion only near 29 eV (see main text Fig. 2b).

SPIN-ORBIT COUPLING IS RESPONSIBLE FOR THE UNIQUE DIRAC-LIKE DISPERSION BEHAVIOUR OF THE BULK BANDS NEAR E_F

According to theoretical models, a strongly spin-orbit coupled bulk band structure is necessary for topological surface states to exist[7−11]. Therefore it is important to show that our

experimentally measured bulk band structure of $Bi_{0.9}Sb_{0.1}$ can only be accounted for by calculations that explicitly include a large spin-orbit coupling term. As shown in the previous section, the measured bulk band dispersion of $Bi_{0.9}Sb_{0.1}$ generally follows the calculated bulk bands of pure Bi from a tight binding model. The dispersion of the bulk valence and conduction bands of pure bismuth near E_F at the L point from such a tight binding calculation[22] with a spin-orbit coupling constant of 1.5 eV are shown in Fig. S3b and c, which show a high degree of linearity. The high degree of linearity can be understood from a combination of the large Fermi velocity ($v_F \approx 6$ eV Å along k_y) and small inter-band (below E_F) gap $\Delta = 13.7$ meV (Fig. S3). This calculated inter-band gap of Bi (13.7 meV) is smaller than our measured lower limit of 50 meV (main text Fig. 1a) for the insulating gap of $Bi_{0.9}Sb_{0.1}$. To illustrate the importance of spin-orbit coupling in determining the band structure near L, we show the dispersion along k_y and k_z calculated without spin-orbit coupling (Fig. S3d and e). While the dispersion along k_z is not drastically altered by neglecting the spin-orbit coupling, the dispersion along k_y changes from being linear to highly parabolic. This is further evidence that our measured Dirac point can be accounted for only by including spin-orbit coupling. *A strong spin-orbit coupling constant acts as an internal quantizing magnetic field for the electron system[6] which can give rise to a quantum spin Hall effect without any externally applied magnetic field[3,4,5,12,37]. Therefore, the existence or the spontaneous emergence of the surface or boundary states does not require an external magnetic field.*

MATCHING THE SURFACE STATE FERMI CROSSINGS AND THE TOPOLOGY OF THE SURFACE FERMI SURFACE IN BULK INSULATING $Bi_{0.9}Sb_{0.1}$

In order to count the number of singly degenerate surface state Fermi crossings[24,28,38] along the $\bar{\Gamma}$-$\bar{M}$ cut of the surface BZ, high photon energy ARPES scans, which allow mapping of the entire k range from $\bar{\Gamma}$-$\bar{M}$ to fall within the detector window at the expense of lower instrument resolution, were taken to preliminarily identify the k-space locations of the Fermi crossings (Fig. S4a). Having determined where these surface state Fermi crossings lie in k-space, we performed several high resolution ARPES scans, each covering a successive small k interval in the detector window, in order to construct a high resolution band mapping of the surface states from $\bar{\Gamma}$ to $\bar{M}$. The second derivative image of the surface band dispersion shown in Fig.S4b was constructed by piecing together four such high resolution scans. Fig.S4c shows energy distribution curves of high resolution ARPES scans in the vicinity of each surface Fermi crossing, which together give rise to the surface Fermi surface shown. No previous work[24,26−30,35,36] has reported the band dispersion near the L-point (thus missing the Dirac bands) or resolved the Kramers point near the $\bar{M}$ point, which is crucial to determine the topology of the surface states. For this reason there is no basis for one-to-one comparison with previous work, since no previous ARPES data exists in the analogous k-range. Note that surface band dispersions along the cuts A, B and C are highly linear. This is indirect evidence for the existence of the bulk Dirac point since surface states are formed when the bulk state wave functions are subjected to the boundary conditions at the cleaved plane.

[1] von Klitzing, K., Dorda, G. & Pepper, M. New method for high-accuracy determination of the fine-structure constant based on quantized Hall resistance. *Phys. Rev. Lett.* **45**, 494-497 (1980).

[2] Tsui, D.C., Stormer, H.L. & Gossard, A.C. Two-dimensional magnetotransport in the extreme quantum limit. *Phys. Rev. Lett.* **48**, 1559-1562 (1982).

[3] Kane, C.L. & Mele, E.J. Quantum spin Hall effect in graphene. *Phys. Rev. Lett.* **95**, 226801 (2005).

[4] Bernevig, B.A. & Zhang, S.-C. Quantum spin Hall effect. *Phys. Rev. Lett.* **96**, 106802 (2006).

[5] Sheng, D.N., Weng, Z.Y., Sheng, L. & Haldane, F.D.M. Quantum spin Hall effect and topological Chern numbers. *Phys. Rev. Lett.* **97**, 036808 (2006).

[6] Haldane, F.D.M. Model for a quantum Hall effect without Landau levels: Condensed-matter realization of the "parity anomaly". *Phys. Rev. Lett.* **61**, 2015-2018 (1988).

[7] Fu, L. & Kane, C.L. Topological insulators with inversion symmetry. *Phys. Rev.* **B76**, 045302 (2007).

[8] Murakami, S. Phase transition between the quantum spin Hall and insulator phases in 3D: emergence of a topological gapless phase. *New. J. Phys.* **9**, 356 (2007).

[9] Fu, L., Kane, C.L. & Mele, E.J. Topological insulators in three dimensions. *Phys. Rev. Lett.* **98**, 106803 (2007).

[10] Moore, J.E. & Balents, L. Topological invariants of time-reversal-invariant band structures. *Phys. Rev.* **B75**, 121306(R) (2007).

[11] Roy, R. Three dimensional topological invariants for time reversal invariant Hamiltonians and the three dimensional quantum spin Hall effect. Preprint at ⟨http://arxiv.org/abs/cond-mat/0607531⟩ (2006).

[12] Bernevig, B.A., Hughes, T.L. & Zhang, S.-C. Quantum spin Hall effect and topological phase transition in HgTe quantum wells. *Science* **314**, 1757-1761 (2006).

[13] König, M. *et al.* Quantum spin Hall insulator state in HgTe quantum wells. *Science* **318**, 766-770 (2007).

[14] Wolff, P.A. Matrix elements and selection rules for the two-band model of bismuth. *J. Phys. Chem. Solids* **25**, 1057-1068 (1964).

[15] Fukuyama, H. & Kubo, R. Interband effects of magnetic susceptibility. II. Diamagnetism of bismuth. *J. Phys. Soc. Jpn.* **28**, 570-581 (1970).

[16] Buot, F.A. Weyl transformation and the magnetic susceptibility of a relativistic Dirac electron gas. *Phys. Rev.* **A8**, 1570-1581 (1973).

[17] Lenoir, B. *et al.* Bi-Sb alloys: an update. *Fifteenth International Conference on Thermoelectrics*, 1-13 (1996).

[18] Zhang, Y. *et.al.* Experimental observation of the quantum Hall effect and Berry's phase in graphene. *Nature* **438**, 201-204 (2005).

[19] Novoselov, K.S. *et al.* Room temperature quantum Hall effect in graphene. *Science* **315**, 1379 (2007).

[20] Zhou, S.Y. *et al.* Substrate-induced bandgap opening in epitaxial graphene. *Nature Mat.* **6**, 770-775 (2007).

[21] Behnia, K., Balicas, L. & Kopelevich, Y. Signatures of electron fractionalization in ultraquantum bismuth. *Science* **317**, 1729-1731 (2007).

[22] Liu, Y. & Allen, E. Electronic structure of semimetals Bi and Sb. *Phys. Rev.* **B52**, 1566-1577 (1995).

[23] Hebel, L.C. & Smith, G.E. Interband transitions and band structure of a BiSb alloy. *Phys. Lett.* **10**, 273-275 (1964).

[24] Kane, C.L. & Mele, E.J. Z_2 topological order and the quantum spin Hall effect. *Phys. Rev. Lett.* **95**, 246802 (2005).

[25] Ast, C.R. & Hochst, H. Fermi Surface of Bi(111) Measured by Photoemission Spectroscopy. *Phys. Rev. Lett.* **87**, 177602 (2001).

[26] Hochst, H. & Gorovikov, S. Lack of electron-phonon coupling along two-dimensional bands in $Bi_{1-x}Sb_x$ single crystal alloys. *J. Elect. Spectrosc. Relat. Phenom.* **351**, 144-147 (2005). This work does not measure the surface state along the critical $\bar{\Gamma} - \bar{M}$ direction or detect the bulk Dirac spectrum near L.

[27] Hofmann, P. The surfaces of bismuth: Structural and electronic properties. *Prog. Surf. Sci.* **81**, 191-245 (2006).

[28] Hirahara, T. *et al.* Direct observation of spin splitting in bismuth surface states. *Phys. Rev.* **B76**, 153305 (2007).

[29] Hengsberger, M. *et al.* Photoemission study of the carrier bands in Bi(111). *Eur. Phys. J.* **17**, 603-608 (2000).

[30] Ast, C.R. & Hochst, H. Electronic structure of a bismuth bilayer. *Phys. Rev.* **B67**, 113102 (2003).

[31] Kopelevich, Y. *et al.* Universal magnetic-field-driven metal-insulator-metal transformations in graphite and bismuth. *Phys. Rev.* **B 73**, 165128 (2006).

[32] Hufner, S. Photoelectron Spectroscopy (Springer, Berlin, 1995).

[33] Novoselov, K. S. *et al.* Two-dimensional gas of massless Dirac fermions in graphene. *Nature* **438**, 197-200 (2005).

[34] Bostwick, A., Ohta, T., Seyller, T., Horn, K. & Rotenberg, E. Quasiparticle dynamics in graphene. *Nature Phys.* **3**, 36-40 (2007).

[35] Jezequel, G., Thomas, J. & Pollini, I. Experimental band structure of semimetal bismuth. *Phys. Rev.* **B 56**, 6620-6626 (1997).

[36] Ast, C. R. & Hochst, H. High-resolution mapping of the three-dimensional band structure of Bi(111). *Phys. Rev.* **B 70**, 245122 (2004).

[37] Sheng, L., Sheng, D. N., Ting, C. S. & Haldane, F. D. M. Nondissipative spin Hall effect via quantized edge transport. *Phys. Rev. Lett.* **95**, 136602 (2005).

[38] Kim, T. K. *et al.* Evidence against a charge density wave on Bi(111). *Phys. Rev.* **B 72**, 085440 (2005).

[39] Hsieh, D., Hasan, M.Z. *et al.* Observation of unconventional quantum spin textures in topological insulators. *Science* **323**, 919 (2009).